npj | biomedical innovations

Article

https://doi.org/10.1038/s44385-024-00006-6

# Bacterial hitchhiking with drug-loaded nanoparticles as a drug delivery strategy for cancer immunotherapy



Radu A. Paun[1,2], Daciana C. Dumut[2,3], Ling Li[1], Danuta Radzioch[2,3,4] & Maryam Tabrizian[1,5] ✉

Select strains of bacteria show significant therapeutic promise in oncology, but there are major limitations for their clinical implementation, including their fast clearance from the circulation and dose-limiting toxicity. To address this challenge, we propose delivering bacteria alongside drug-loaded nanoparticles to reduce the premature clearance of bacteria from the circulation and improve their therapeutic efficacy. We evaluated the ability of the bacterium *Magnetospirillum gryphiswaldense*, an environmental isolate that holds promise as an anti-cancer immunotherapy, to carry drug-loaded nanoliposomes into melanoma tumors. Using the B16F10 melanoma mouse model, we demonstrated that when injected locally, the bacteria can significantly reduce tumor growth while inducing a strong immune response. Further, we showed that drug-loaded nanoliposomes can be conjugated to the surface of bacteria improving their tumoral delivery and yielding a stronger anticancer response when delivered systemically. These results suggest that bacterial hitchhiking is a promising systemic drug delivery strategy for cancer immunotherapy.

Recent advances in the field of immunotherapy have enabled the development of a novel class of cell based (living) therapeutics for the treatment of cancer. For example, the production of chimeric antigen receptor (CAR) T cells has substantially transformed the treatment of hematologic malignancies by improving patient outcomes[1]. Over the years, multiple studies have shown that both strict and facultative anaerobic bacteria, including but not limited to *Clostridium novyi*, *Listeria monocytogenes*, *Escherichia coli*, and *Salmonella enterica* can actively target and colonize solid tumors in mouse models of cancer given the presence of a favorable tumor microenvironment[2,3]. Due to their malignant transformation, cancer cells can significantly modify their surrounding environment resulting in the presence of hypoxic regions and lower pH inside the tumor mass. This results in an overall immunosuppressive environment within a tumor, giving rise to conditions that can accommodate the growth of certain bacteria and enable more efficient colonization of tumor lesions that are as small as five cell layers thick[4]. Furthermore, previously published studies have demonstrated that bacteria, and bacterial derived products, have potent anti-neoplastic activity *via* the activation of the immune system and the expansion of $CD4^+$ and $CD8^+$ T cells through toll-like receptor (TLR) and cytokine signaling[5–8]. Given the ability of bacteria to use their flagella for propulsion, they can achieve improved tumoral tissue biodistribution profiles compared to viruses, activating and recruiting immune cells deeper into tumors[9,10]. In addition, bacteria are not limited by the presence of viral immunodominance, which can skew the immune response towards viral antigens that replicate in cancer cells, as is the case for oncolytic viruses. Aside from their immunostimulatory properties, bacteria can also be genetically or chemically engineered to deliver and release therapeutic payloads directly at the site of the lesion in a controlled manner[11]. For example, Chowdhury et al. were able to engineer *E. coli* to release nanobodies designed to work as immune checkpoint inhibitors (ICI) directly into the tumor tissue using a genetically encoded lysis circuit[12]. Our group, and others, have shown that drugs/nanoparticles can be loaded into/onto various types of bacteria, thereby working as self-propelled therapeutic agents that can deliver drugs to tumors, a concept known as cell hitchhiking[13–20]. However, thus far, only the live *Mycobacterium bovis* vaccine Bacillus Calmette Guerin (BCG) has resulted in successful clinical trials for the localized treatment of superficial bladder cancer. A major limitation for bacterial-based cancer therapeutics is their inability to robustly colonize metastatic tumors that are not amenable for localized therapy when injected intravenously (IV) into humans[21]. Highly motile bacterial populations are required for active targeting and colonization through the circulation, a consideration that has not been addressed prior to human trials[22,23]. Another

[1]Department of Biomedical Engineering, Faculty of Medicine and Health Sciences, McGill University, Montreal, Canada. [2]Research Institute of the McGill University Health Centre, Montreal, Canada. [3]Department of Medicine, Faculty of Medicine and Health Sciences, Montreal, Canada. [4]Department of Human Genetics, Faculty of Medicine and Health Sciences, Montreal, Canada. [5]Faculty of Dentistry and Oral Health Sciences, McGill University, McGill University, Montreal, Canada. ✉e-mail: maryam.tabrizian@mcgill.ca

important issue is the fast opsonization and clearance of attenuated bacteria from the blood by scavenger cells in the liver and spleen following IV infusions of non-toxic doses ($< 10^9$ CFU/m$^2$)[24–26]. Lastly, convincing evidence in patients shows a significant upregulation of multiple immune checkpoints in the later stages of sepsis as a result of the inflammatory response, which could be a contributing factor to the observed immune resistance of tumors when bacteria are administered as monotherapy[27,28].

To address some of these challenges, and to complement the therapeutic benefit of bacterial-mediated immune activation, we propose to use nanoparticle-drug payloads in combination with bacterial vectors to improve the delivery and efficacy of bacterial-based immunotherapies. This strategy uses drug-loaded nanoparticles to improve the bacterial biodistribution profile once in the circulation, as well as to complement their anti-cancer efficacy. Nanoparticles surround and attach onto the bacterial surface to temporarily reduce the phagocytic rate of the bacteria by scavenger cells and allow for better tumor colonization and an improved anti-cancer immune response (Fig. 1).

For example, nanoparticles have the ability to change their pharmacokinetic profile in circulation in a dose dependent manner, whereby if more than $10^{12}$ nanoparticles are administered IV to a mouse, enough particles can saturate scavenger cells and reduce the overall liver clearance of the remaining circulating nanoparticles[29]. For this strategy to be effective, circulating nanoparticles should bind to scavenger cells through similar receptors as the bacteria. In our case, attaching the nanoparticles to the bacterial surface could improve the bacterial stealth properties due to the presence of polyethylene glycol (PEG) on the nanoparticles, thereby increasing their circulation time and tumor delivery. To apply this concept to bacterial-based cancer therapeutics, we have chosen the bacterium *Magnetospirillum gryphiswaldense* strain MSR-1 as an immunotherapy candidate due to its robust swimming abilities (10–20 µm/s) and potential to target and colonize tumor hypoxic regions in mice, as *Magnetospirillum* bacteria are known microaerophiles with the ability to colonize tumors[30]. Furthermore, *Magnetospirillum* bacteria have been shown to induce apoptosis in cancer cells and sequester large amounts of iron from their environment creating a significant iron pool[31–35]. Iron sequestration and/or overload can sensitize cells to ferroptosis and alter cancer cell gene expression profiles to increase their susceptibility to immune-mediated clearance, particularly by natural killer (NK) cells and macrophages[36,37]. Additionally, bacteria could drive an immune response *via* the agonism of multiple TLRs, which can result in better immune activation compared to individual TLR stimulation alone[38,39]. Nanoliposomes loaded with the metal complex copper diethyldithiocarbamate (CuET) were chosen for the hitchhiking strategy. CuET is a potent inhibitor of the p97-NPL4 protein complex, which is involved in the trafficking of misfolded proteins from the endoplasmic reticulum (ER) to the proteasome[40,41]. Additionally, p97 has multiple cellular roles, such as the regulation of spindle disassembly at the end of mitosis[42–44]. Its inhibition leads to the formation of protein aggregates and the induction of ER stress, which has been shown to cause cytotoxicity in cancer cells[45,46].

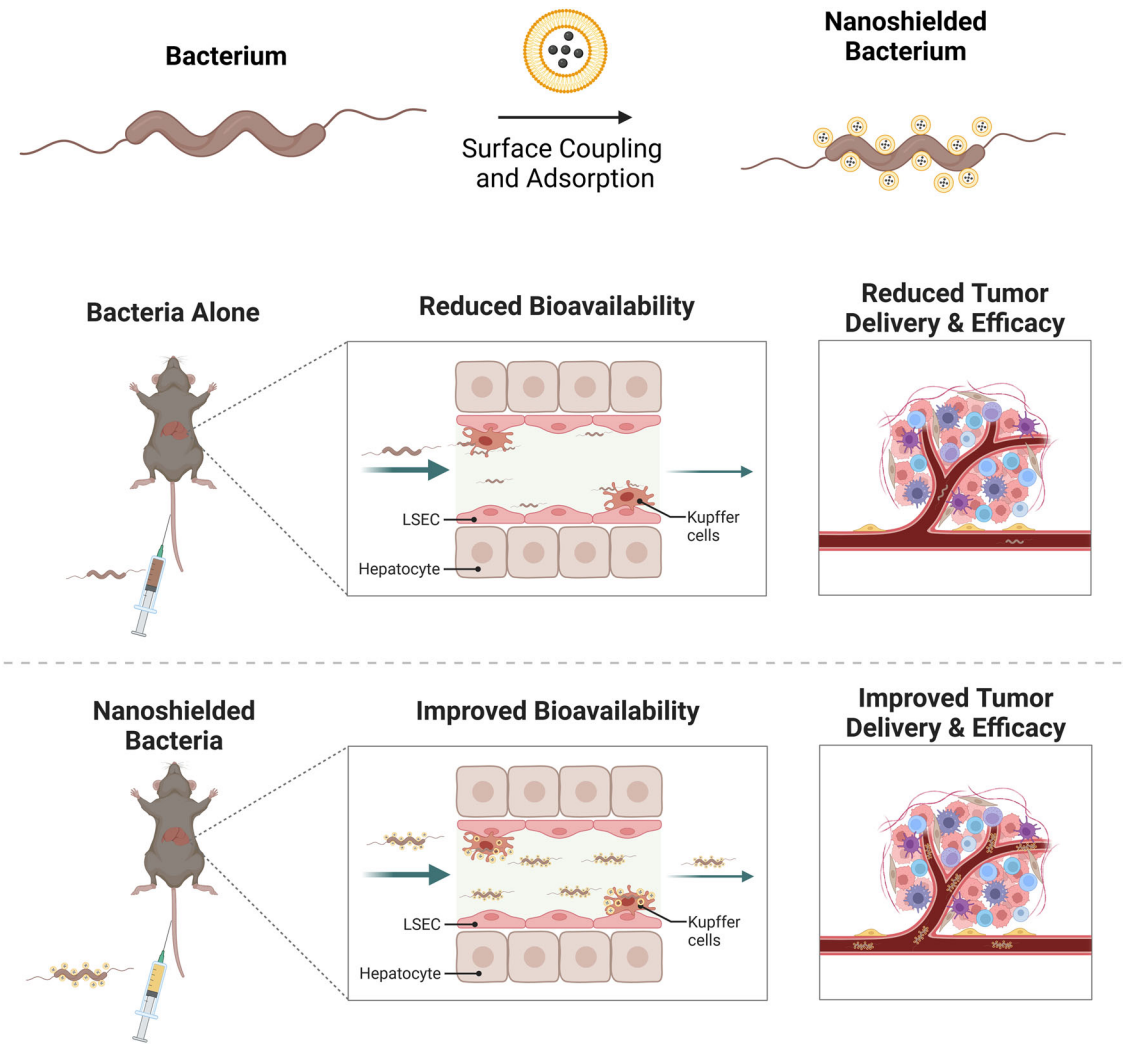


**Fig. 1 | Schematic representation of the bacterial hitchhiking effect.** By using bacteria to transport nanoparticles, more bacteria and drug-loaded nanoparticles can infiltrate tumors and exert a more potent effect. Created in BioRender.com.

Since some melanomas are refractory to immunotherapy (e.g., uveal melanoma), and others can acquire resistance, developing novel treatment methods remains a significant unmet need[47]. We first evaluated the ability of MSR-1 bacteria to induce a potent immunomodulatory effect in a B16F10 mouse model of melanoma that is insensitive to currently approved ICI immunotherapies (i.e., αPD1 and αCTLA4 antibodies). We then developed a bacterial nanoparticle surface capture and adsorption strategy using triazine chemistry to help shelter the bacteria from quick opsonization and phagocytosis, as well as to deliver CuET to scavenging cells that do end up engulfing the bacterial complex. We evaluated the bacterial-nanoparticle complex stability, its uptake by macrophages, and the bacteria's ability to deliver complexed nanoparticles deep inside cancer spheroid models using YUMM 1.7 cells due to their amelanotic features. Finally, we evaluated the efficacy of our delivery strategy in a highly metastatic lung mouse model of B16F10 melanoma. Melanoma was chosen as the preliminary cancer model, since clinically advanced cutaneous melanomas are often metastatic, and they can respond well to immunotherapies, as demonstrated by regulatory approvals for the treatment of melanoma using oncolytic viruses and ICI[48,49].

## Results

### MSR-1 bacteria reduce the growth of B16F10 tumors and activate the immune system

The ability of MSR-1 bacteria to inhibit tumor growth was first assessed in an ectopic B16F10 model of melanoma, previously shown to be insensitive to ICI (Fig. 2A). Results showed that a single peritumoral (PT) injection of $10^8$ CFUs of MSR-1 bacteria can substantially reduce the growth rate of B16F10 tumors in mice compared to PBS, as well as compared to a single PT injection containing $10^8$ CFUs of *E. coli* DH5α as control bacteria (Fig. 2B). The mice also exhibited a significantly longer survival time compared to the two other control groups, as shown in Fig. 2C. The efficacy of treating tumor bearing mice was further evaluated using intraperitoneal (IP) injections of the standard of care ICI (αPD1 + αCTLA4) or isotype control antibodies

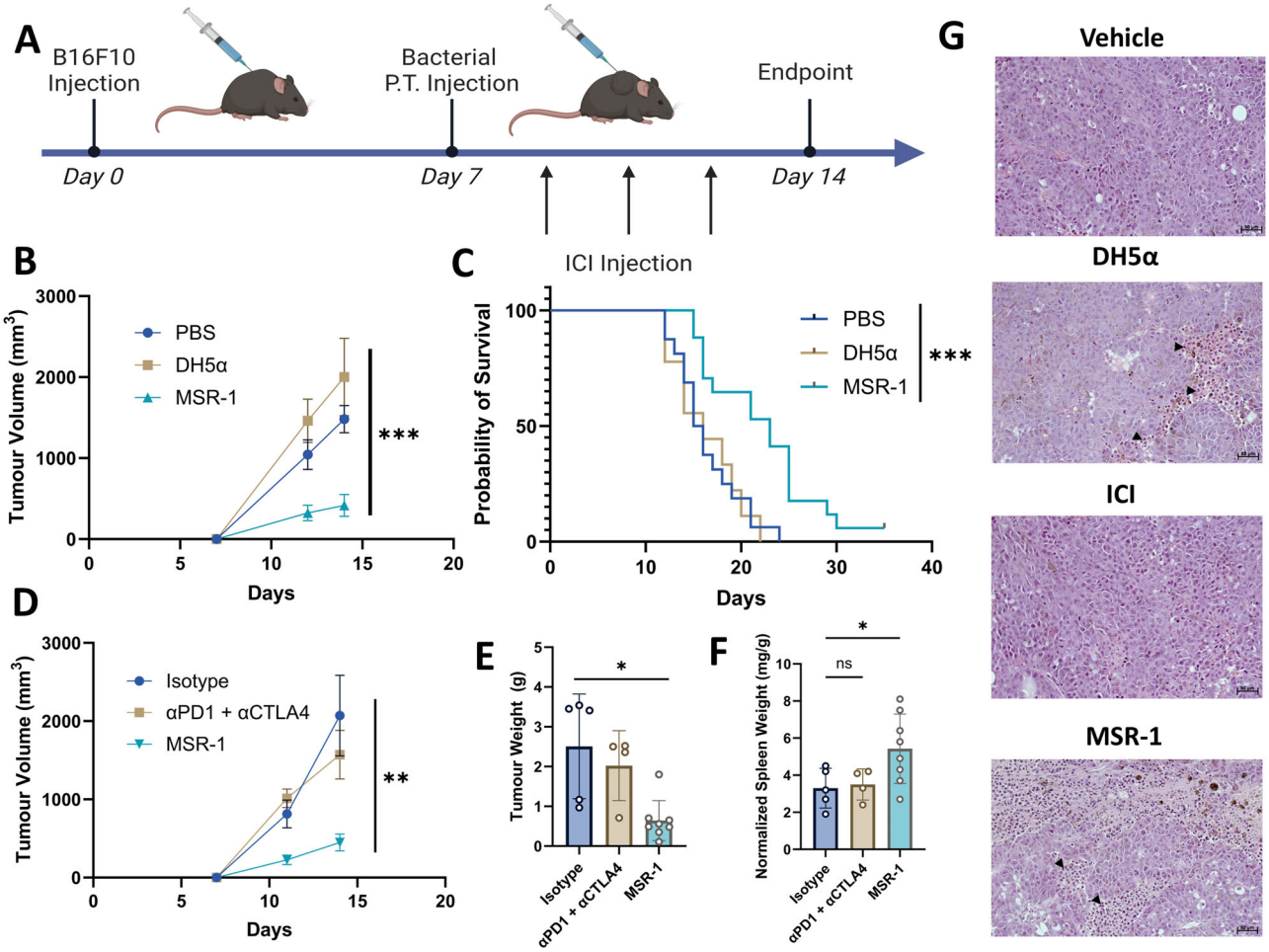


**Fig. 2 | MSR-1 bacteria reduce the growth of B16F10 melanoma. A** Experimental setup and mouse treatment schedule. C57BL/6 mice bearing ectopic B16F10 tumors are treated on day 7 peritumorally (PT) with PBS ($n = 15$), $10^8$ CFU E. coli DH5α ($n = 9$) and $10^8$ CFU M. gryphiswaldense MSR-1 ($n = 17$) in one set of experiments, and with $10^8$ CFU M. gryphiswaldense MSR-1 ($n = 8$), or intraperitoneal injections of 100 μg of IgG isotype controls ($n = 5$), 100 μg of αPD-1 + 100 μg of αCTLA-4 antibody ($n = 4$) in another set of experiments. **B** Tumor growth kinetics of treated mice showing a significant reduction in tumor volume in mice treated with MSR-1 compared to DH5α or PBS controls; student's t-test with Welch's correction was used at day 14; data from two pooled experiments shown as mean ± SEM. **C** Kaplan–Meier survival analysis showing the increased survival of mice treated with MSR-1 compared to DH5α or PBS controls; the log-rank test was used. **D** Tumor growth kinetics of treated mice showing a significant reduction in tumor volume in mice treated with MSR-1 compared to standard of care αPD-1 + αCTLA-4 or isotype controls; student's t-test with Welch's correction was used at endpoint; data as mean ± SEM. **E** Tumor weight comparison amongst the different treatment groups at endpoint showing the reduction in the MSR-1 group; student's t-test with Welch's correction was used at endpoint; empty circles represent individual mice, and data as mean ± SD. **F** Comparison of the difference in the spleen weight normalized to the mouse body weight between the treatment groups showing a larger spleen weight in mice treated with MSR-1; student's t-test with Welch's correction was used at endpoint; empty circles represent individual mice, and data as mean ± SD. **G** Hematoxylin and eosin staining of tumor sections from different treatment groups showing the immune infiltrates (black arrows) present in the bacterial treatment groups.

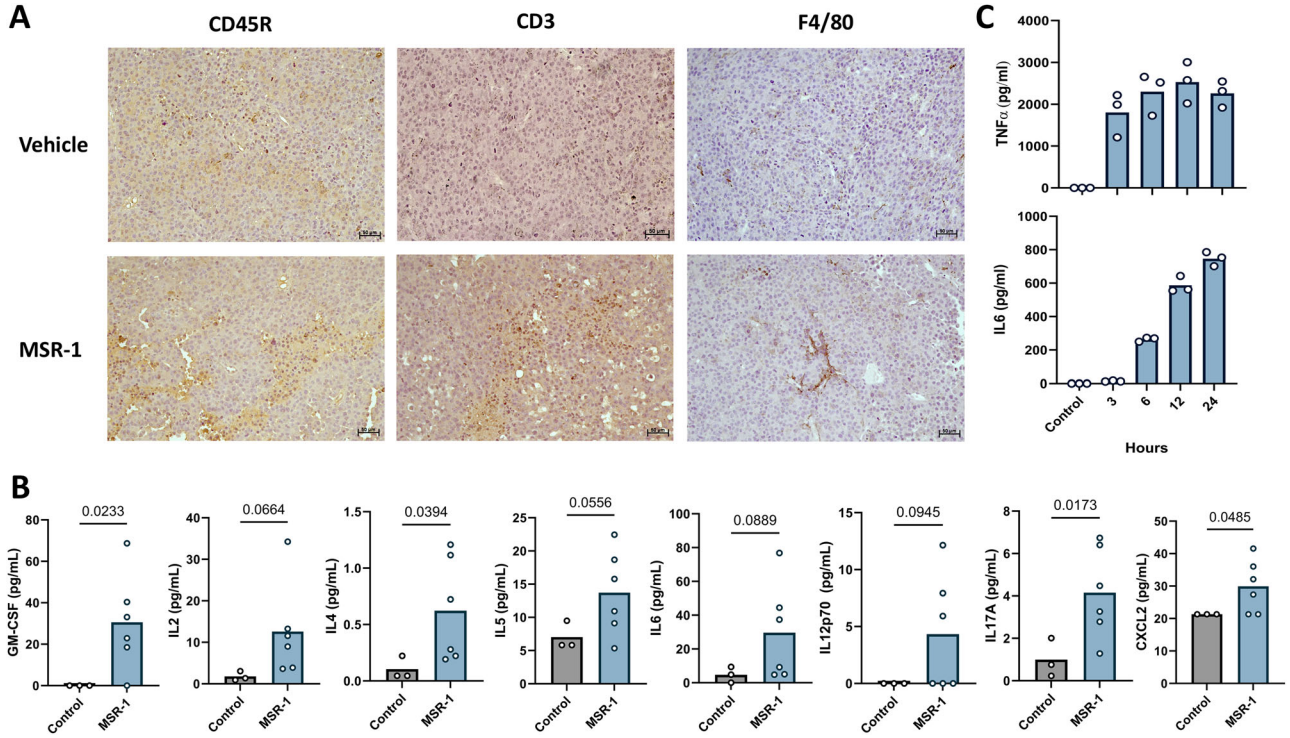


**Fig. 3 | MSR-1 bacteria induce a potent immune response.**
**A** Immunohistochemistry images show an increase in CD45R$^+$, CD3$^+$, and F4/80$^+$ cell infiltrates in the tumor microenvironment of the MSR-1 treated group. Scale bars are 50 µm. **B** Difference in cytokine levels in isolated mouse serum between PBS control ($n = 3$) and $10^8$ CFU of MSR-1 ($n = 6$) treated groups using the Luminex assay at 24 h post peritumoral injection showing a notable increase in inflammatory cytokines and chemokines; student's t-test with Welch's correction was used; empty circles represent individual mice and data is shown as mean. **C** THP-1 cells were treated with MSR-1 bacteria at a ratio of 1:10 in vitro showing a time-dependent increase in TNFα and IL-6 secretion; empty circles represent individual experiments, and data is shown as mean.

and compared to a single PT injection of $10^8$ CFU of MSR-1 bacteria. In this case, MSR-1 bacteria showed a clear advantage with respect to the reduction of tumor growth (Fig. 2D), as well as a reduction of the tumor weight at endpoint (Fig. 2E), replicating the observations seen in the previous experiments with *E. coli*. The mice demonstrated consistent tumor growth kinetics depending on the administered treatment in all respective subgroups across experiments without any noticeable organ toxicity (Supplementary Figs. 1,2). These results are intriguing as MSR-1 bacteria have never been employed before as immunomodulators in cancer models, and the bacteria seem to have a strong effect on reducing tumor growth beyond a typical bacterial TLR stimulation, as the same effect was not replicated when *E. coli* were used to treat the mice. Indeed, MSR-1 bacteria have a distinct genome with a higher GC content (63%) and an innate ability to store large amounts of iron deposits (Supplementary Figs. 3–6), roughly 2% of the bacterial weight compared to *E. coli* at 0.05%[31–33]. In line with these expectations, a significant increase in the weight of mouse spleens was observed when normalized to the mouse body weight in groups treated with MSR-1 bacteria as shown in Fig. 2F, as well as an increase in cellular infiltrates on H&E-stained tumor sections compared to other treatment groups (Fig. 2G); only the DH5α group showed a noticeable increase in infiltrates, but less pronounced than in the MSR-1 group.

Immunohistochemistry staining on tumor sections from PBS and MSR-1 treated mice was performed to identify the type of cellular infiltrates in the treated tumors. Results indicated a marked increase in the presence of CD45R, CD3 and F4/80 positive cells, which are surrogate markers for B cells, T cells, and macrophages, respectively as shown in Fig. 3A. The increase in tumor infiltrating lymphocytes (TIL) is an important marker, as these infiltrates are associated with better response rates in patients undergoing ICI therapy[50]. The protective effect, established by the treatment of tumor-bearing mice with MSR-1 bacteria, seems to be associated not only with a noticeable increase in TILs, but also with the increased presence of inflammatory cytokines in mouse plasma (Fig. 3B) that may contribute to the anti-cancer immune response. Interestingly, there was a trending increase in IL-13, and a few other differences were detected between treated and control groups in other plasma cytokine levels as illustrated in Supplementary Fig. 7. However, M0 THP-1 macrophages stimulated with MSR-1 bacteria are able to produce large amounts of TNFα with a gradual increase in IL-6 production over a period of 24 h in vitro (Fig. 3C). A significant limitation of bacterial-based cancer therapeutics is their fast clearance from the circulation when injected IV before they can exert an impact on the tumor microenvironment, which was confirmed by treating tumor-bearing mice IV with one injection of $10^9$ CFUs showing no significant difference in the tumor size at endpoint (Supplementary Fig. 8). To address this issue, and to improve the therapeutic effect of IV injected bacteria, we sought to use nanoparticles as an additional therapeutic layer to complement the observed bacterial effect.

## Drug-loaded nanoparticles can be complexed to MSR-1 bacteria using triazine chemistry

Additionally, coupling nanoparticles to bacterial surfaces could also confer some form of stealth properties against scavenger cells, if the nanoparticles themselves are stealth, like in the case of PEG-containing nanoliposomes (LP). Figure 4A displays a schematic of the drug-containing PEGylated liposomes on the surface of bacteria bound *via* triazine chemistry, due to the abundance of amine and hydroxyl groups present on the bacterial outer membrane. This strategy was used to attach the nanoliposomes encapsulating copper diethyldithiocarbamate (LP-CuET), a metal complex that has shown promise as an anti-cancer agent, to stimulate the immune response (Supplementary Fig. 9)[51,52]. Scanning electron microscopy (SEM) imaging (Fig. 4B) shows the successful coupling of LP-CuET to bacteria, which was further confirmed by fluorescence microscopy using fluorescently tagged liposomes (Fig. 4C). To quantify the number of LP-CuET particles attached

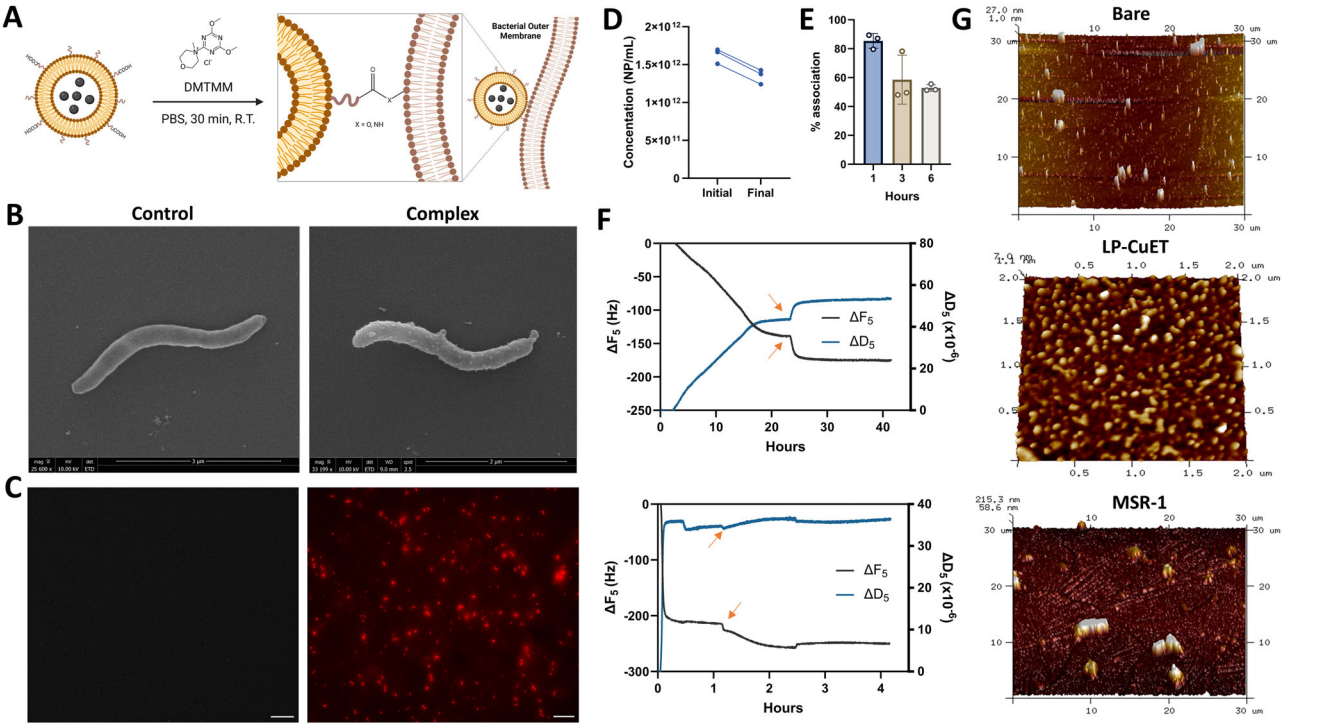


**Fig. 4 | Drug-loaded nanoparticles can be complexed to MSR-1 bacteria using triazine chemistry. A** Schematic representation of CuET-loaded liposome (LP-CuET) attachment to the surface of bacteria using triazine chemistry. **B** Scanning electron microscopy images showing control bacteria (left) and bacteria with captured LP-CuET on the surface (right). **C** Fluorescence microscopy images showing the capture of fluorescently labeled liposomes (right) on the bacteria compared to control bacteria (left). Scale bars are 20 µm. **D** Concentration of LP-CuET in solution as measured by nanoparticle tracking analysis before being captured by bacteria (Initial) compared to after capture (Final). **E** Stability of captured liposomes onto bacteria with respect to time showing the bacterial shedding of nanoparticles; empty circles represent individual experiments, and data is shown as mean ± SD. **F** Quartz crystal microbalance with dissipation (QCMD) experiments showing that bacteria can adsorb onto activated $SiO_2$ sensors and capture LP-CuET once they start flowing onto the sensor (upper graph, arrows). Similarly, when LP-CuET is captured onto the surface first, bacteria attach to the particles once they start flowing onto the sensor (lower panel, arrows). **G** Atomic force microscopy images showing the QCMD sensor surface containing LP-CuET and bacteria captured on LP-CuET nanoparticles.

to the bacteria, the number of particles in solution leftover after coupling to the bacteria was determined (Final = $1.35 \times 10^{12}$ np/mL) and then subtracted from the amount before coupling (Initial = $1.62 \times 10^{12}$ np/mL) (Fig. 4D), which yielded $2.77 \times 10^{11}$ LP-CuET liposomes coupled to $10^9$ CFU of bacteria without any intrinsic toxicity to the bacteria itself (Supplementary Fig. 10). Therefore, there are approximately 277 nanoparticles attached per bacterium, which is in line with the SEM data.

To evaluate the stability of surface-captured nanoparticles, we quantified their release from the bacterial surface in a PBS solution using nanoparticle tracking analysis (NTA) over a period of 6 h post-coupling (Fig. 4E). Roughly 50% of LP-CuET particles remain attached to the bacterial surface after 6 h, but the particles start being released within 3 h after coupling, suggesting that for maximum efficiency, the nanoplexed bacteria should be administered within one hour post coupling. Reasons for nanoparticle shedding are numerous, but they can involve the cleaving of the nanoparticle anchor from their attachments on the bacterial surface or the shedding of outer membrane vesicles (OMVs) that MSR-1 bacteria can release in the supernatant (Supplementary Fig. 11). Interestingly, when the bacteria are adsorbed onto a substrate, as would be the case for their interactions with mammalian cells or tissues, the bacterial-nanoparticle coupling seems to be more stable. This was shown by adsorbing bacteria onto poly-L-lysine coated $SiO_2$ quartz crystal microbalance with dissipation (QCMD) sensors until a stable cell monolayer was achieved (Supplementary Fig. 12) onto which DMTMM-activated LP-CuET was flown to evaluate their capture directly onto the bacteria as shown in the top graph in Fig. 4F. The captured liposomes were stable for over 20 h on the surface. This was also the case when bacteria were captured directly onto a surface pre-coated with DMTMM-activated liposomes (bottom graph). When liposomes were not DMTMM-activated, the bacteria were readily detached from the surface (Supplementary Fig. 13). These results were confirmed by atomic force microscopy (AFM) imaging showing the bacteria captured directly onto LP-CuET liposomes on a poly-L-lysine glass slide (Fig. 4G). These results suggest that bacteria are likely to be taken up by cells alongside the drug-loaded nanoparticles, which could end up increasing the amount of drug delivery to cells that uptake the bacterial nanoplex.

## MSR-1 bacteria target melanoma tumors and help deliver drug-loaded nanoparticles

To test whether MSR-1-LP-CuET complexes (MLC) could alter the delivery of nanoparticles into tumor tissue, we utilized 3D spheroids composed of YUMM 1.7 cells as a delivery and distribution model. When the spheroids were treated using fluorescent liposomes alone, there was a diffuse distribution of the liposomes, predominately located towards the periphery of the spheroids, whereas both RBITC-labeled bacteria and the MLC complex tagged with fluorescent liposomes alone showed a significant accumulation towards the core of the spheroid (Fig. 5A, B, Supplementary Figs. 14-15). Importantly, for the MLC group, only the liposomes were fluorescently labeled, indicating that they are directly transported into the core of the spheroids *via* the bacterial vectors without major detachment along the way. Further, the ability of macrophages, an important part of the mononuclear phagocytic system (MPS), to uptake bacteria with or without conjugated nanoparticles was evaluated. There is a significant decrease in the phagocytosis of bacteria by M0 THP-1 cells in the MLC group as compared to the naked MSR-1 bacteria (Fig. 5C). Interestingly, this effect is much more significant when CuET is encapsulated in the liposomes compared to empty liposomes alone (Fig. 5C, Supplementary Fig. 16). This indicates that while the presence of surface-conjugated empty liposomes seems to somewhat reduce the uptake of bacteria from the media, having CuET present

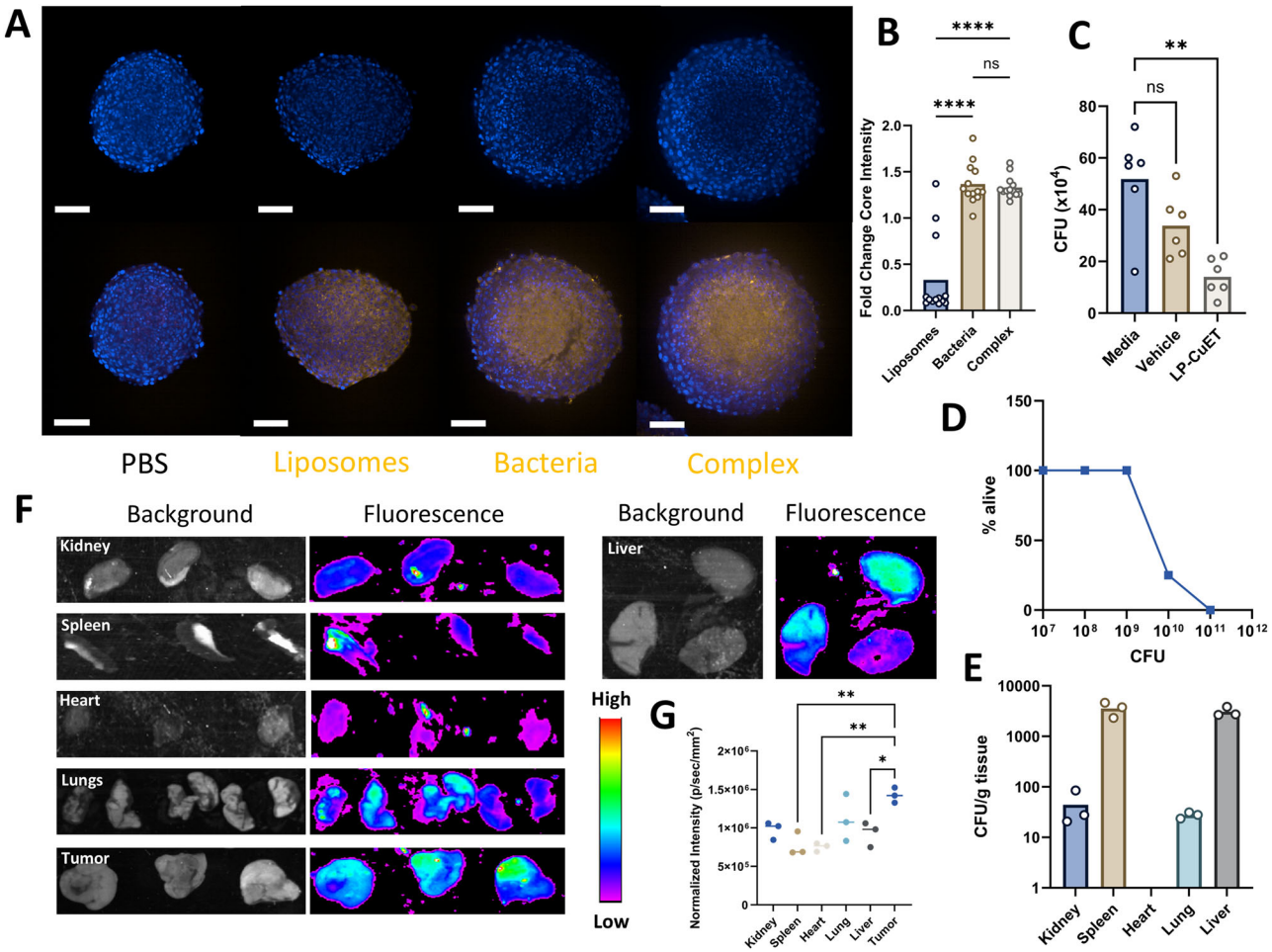


**Fig. 5 | MSR-1 bacteria are well tolerated in mice and can colonize tumors.** **A** Confocal microscopy images of central sections of YUMM 1.7 spheroids showing the distribution of fluorescently tagged liposomes, bacteria, and the complex. Only the liposomes were fluorescently tagged for the complex group. Scale bar is 100 µm. **B** Quantification of spheroid core fluorescence intensity of the nanoparticles or bacteria that penetrated into the core region of YUMM 1.7 spheroids, quantified by image analysis of spheroids' cross-sections showing that liposomes are delivered alongside bacteria into the core of the spheroids; Welsch's One-Way ANOVA with Dunnett's 3 T correction was used; empty circles represent individual spheroids and data is shown as mean. **C** Phagocytosis experiment showing that treating M0 differentiated THP-1 cells with bacteria and LP-CuET diminishes their phagocytic activity; empty circles represent individual experiments and data is shown as mean. **D** $LD_{50}$ experiment demonstrating the maximum tolerated dose of MSR-1 bacteria that can be systemically administered to mice ($n = 6$), namely around $2 \times 10^8$ CFU/g. **E** Biodistribution of bacteria in mouse organs 7 days after IV injection of $10^8$ CFU showing that bacteria preferentially accumulate in liver and spleen tissue; empty circles represent individual mice and data is shown as mean. **F** Ex vivo fluorescence images of mouse organs showing the accumulation of fluorescently tagged bacteria 6 h after IV injection. **G** Quantification of normalized fluorescence intensity of mouse organs showing the accumulation of bacteria in mouse tumors; circles represent individual mice and data is shown as mean.

significantly reduces the ability of THP-1 macrophages to phagocytose bacteria from the media, therefore compounding the effect of empty liposomes alone without any noticeable toxicity to the THP-1 cells. When THP-1 macrophages were pretreated with DMSO-dissolved CuET (1 µM) for 3 h, the same effect was observed with fluorescent microparticles, namely, there were less microparticles being internalized by macrophages pretreated with CuET (Supplementary Fig. 17). When CuET is added to cells, it triggers an ER stress response to prevent aberrant cell function and death as a result of the accumulation of toxic proteins, which enhance the toxicity of MLC in melanoma cells at a bacteria-to-cancer cell ratio of 10000:1 (Supplementary Fig. 18), but in macrophages, ER stress seems to also reduce their phagocytic ability at non-toxic doses.

The safety of administering MSR-1 intravenously in vivo was assessed by determining the 50% lethal dose ($LD_{50}$) through escalating dose administration in mice. A safely tolerated dose of up to $10^9$ CFUs was determined before any serious adverse events, such as significant weight loss, lethargy, or death would occur (Fig. 5D, Supplementary Fig. 19), consistent with data for other magnetotactic bacteria[20,30]. The bacteria mainly accumulated in the liver and spleen, since these are important organs with respect to the MPS. On day 7, there was a noticeable number of live bacteria still present in the liver and spleen, as well as in the kidneys and lungs (Fig. 5E). However, by day 14 the mice were able to clear the bacteria from their system (data not shown). To evaluate the organ biodistribution profile of fluorescently tagged MLC bacteria ($10^9$ CFU) in vivo, we performed ex vivo imaging of isolated mouse organs and explanted YUMM 1.7 tumors at the 6-hour timepoint (Fig. 5F). We chose to administer $10^9$ CFUs to achieve the maximum dose efficacy that is also tolerated by mice. There was a marked accumulation of MLC bacteria in mouse YUMM 1.7 tumors, to a significantly higher extent than in the mouse liver, heart, or spleen (Fig. 5G).

## Nanoplexed bacteria reduce the tumor burden in a B16F10 metastatic mouse model

Next, the efficacy of the bacterial nanoplex formulation was evaluated according to the treatment schedule in Fig. 6A in a B16F10 lung metastatic melanoma model. Once mice established lung metastases, they received two intravenous injections of empty liposomes, 1 mg/kg LP-CuET, $10^9$ CFUs of MSR-1, and $10^9$ CFUs of MLC. At endpoint, individual tumor nodules that

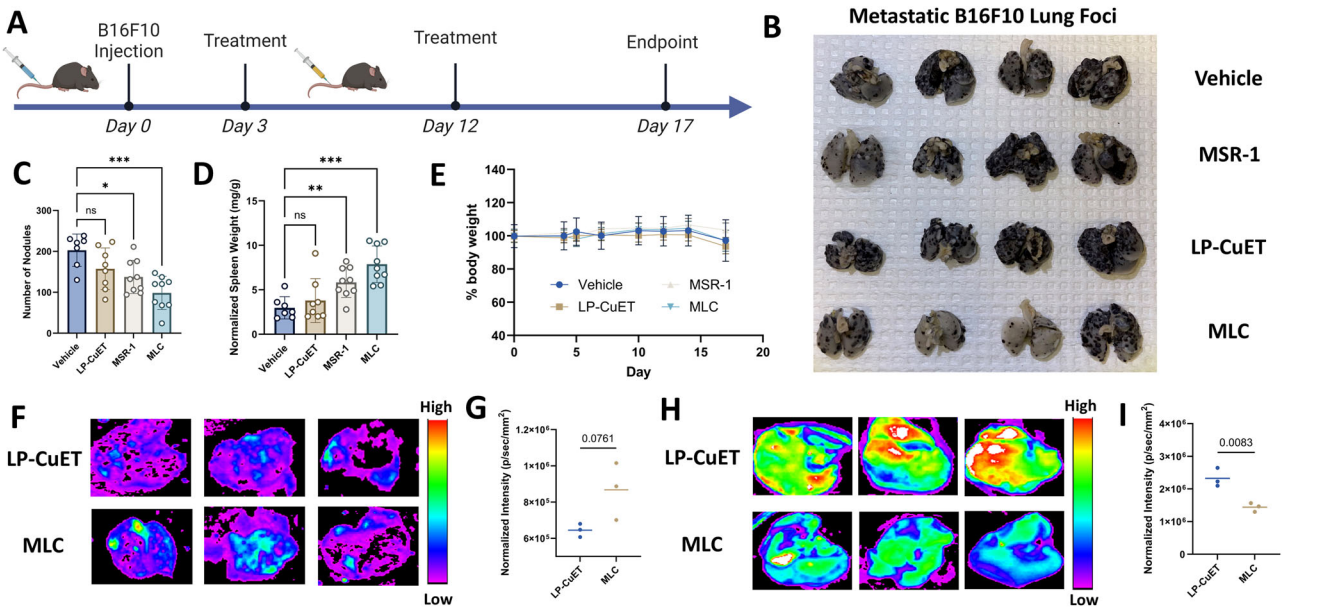


**Fig. 6 | Nanoplexed bacteria improve the treatment of B16F10 lung metastases.** **A** Experimental setup and mouse treatment schedule. C57BL/6 mice bearing B16F10 lung tumors are treated on days 3 and 12 intravenously with vehicle ($n = 7$), 1 mg/kg LP-CuET ($n = 8$), $10^9$ CFU MSR-1 ($n = 9$), and $10^9$ CFU MLC ($n = 9$). **B** Representative lung pictures showing the extent of the tumor burden in each treatment group; black nodules represent individual tumors. **C** Number of lung nodules observed in lung metastases in mice at endpoint; Welsch's One-Way ANOVA with Dunnett's 3 T correction was used; empty circles represent individual mice, and data as mean ± SD. **D** Difference in the spleen weight normalized to the mouse body weight between the treatment groups at endpoint; Welsch's One-Way ANOVA with Dunnett's 3 T correction was used; empty circles represent individual mice, and data as mean ± SD. **E** Change in mouse weight over the course of the treatment. **F** Ex vivo fluorescence images of mouse lungs containing B16F10 melanoma showing the accumulation of fluorescent nanoparticles 6 h after IV injection. **G** Quantification of lung fluorescence intensity; student's t-test with Welch's correction was used; circles represent individual mice, and data presented as mean. **H** Ex vivo fluorescence images of mouse livers showing the accumulation of fluorescent nanoparticles 6 h after IV injection. **I** Quantification of liver fluorescence intensity; student's t-test with Welch's correction was used; circles represent individual mice, and data presented as mean.

formed in the lungs were manually counted (Fig. 6B). The MLC group showed the strongest tumor growth inhibition by the number of nodules present on the lung surface compared to the vehicle control group (Fig. 6C). The MSR-1 group also exhibited a significant reduction in nodule count, but to a lesser extent. In line with these results, the weight of the spleen normalized to the mouse body weight for the MSR-1 and MLC groups were significantly higher than the vehicle control (Fig. 6D) without significant changes in their body weight (Fig. 6E). This finding mirrors the efficacy data obtained using local injections of MSR-1 in subcutaneous B16 F10 models, where the spleen size increased along with efficacy in the treated mice, suggesting that the observed therapeutic effect is likely driven by an anti-cancer immune response. Additionally, when the mice were treated with local injections of CuET or MLC in a subcutaneous model, the efficacy observed with IV administration was not replicated, nor was it improved with the addition of ICI, (Supplementary Fig. 20) in striking contrast to the improvement observed with the systemic treatment of metastatic disease in the MLC group. This is likely due to a strong inflammatory response that is present when CuET is administered locally at high concentrations as noted by the development of erythema and the formation of thickened fibrotic tissue at the injection site (data not shown). In addition, high concentrations of CuET in the tumors could also induce toxicity towards recruited effector immune cells, preventing their tumoricidal function, as well as preventing the activation of a more potent systemic immune response.

Finally, the delivery of fluorescently labeled LP-CuET to tumor-bearing lungs (Fig. 6F, G) and to the liver (Fig. 6H, I) 6-hours post IV injection was assessed. There was a trending increase in the delivery of LP-CuET to tumor-bearing lungs in the presence of MSR-1 bacteria. Even with a small number of mice per group, a significant and consistent decrease in the amount of LP-CuET in the liver in the presence of bacteria compared to MLC group was observed. It is important to note, as mentioned in the Methods section, that B16F10 tumors contain large amounts of melanin, which can block light in the emission range of Texas Red™, making it more difficult to obtain significant fluorescence data from within tumor lesions. Nonetheless, we observe an increase in the number of live bacteria present in B16F10 tumors of mice when the mice are treated IV with MLC compared to MSR-1 alone, as well as the amount of fluorescent LP-CuET present in lesions after IV injections with MLC or LP-CuET when imaged using confocal microscopy (Supplementary Fig. 21).

## Discussion

The use of engineered probiotics in oncology holds significant potential to improve cancer treatments by harnessing bacteria's ability to colonize tumors and stimulate an anti-cancer immune response. While the exact mechanism of action of MSR-1 in the treatment of B16F10 melanoma is not yet entirely understood, there are potential avenues that are worth exploring. For example, the bacterium *M. magneticum* strain AMB-1 was previously shown to behave as a living iron chelator, to reduce cancer cell proliferation, and to strongly induce apoptosis under hypoxic conditions in vitro[34,35]. However, a significant decrease in the proliferative index was observed at or above a ratio of cancer to bacterial cells of 1:1000, which is consistent with our observations for the MSR-1 strain in melanoma cells. Changes in iron metabolism have also been implicated in immunomodulation where chelation can lead to improvements in the ability of NK cells to clear cancer cells *via* specific receptor expression[37]. Alternatively, iron overload as a result of dead bacterial cells, or their iron-containing molecular products, being engulfed by tumor cells could potentially sensitize the cells to ferroptosis and further modulate the anti-cancer immune response, which could lead to slower tumor growth[35,53].

In addition to iron's immunomodulatory effects, bacteria contain various pathogen associated molecular patterns (PAMPs) that are recognized by TLRs on immune cells to promote an inflammatory response. Notably, increases in IL-2 and IL-17A are typically driven by activated $T_h17$ cells, and the presence of IL-4 and IL-5 secretion is associated with a $T_h2$ response to establish humoral immunity, both led by $CD4^+$ T cells against

extracellular pathogens[54–56]. Interestingly, IL-4 and IL-5 cytokines, in a $T_h2$-directed immune response, can play an important protective role in the context of anti-tumor immunity, particularly in melanoma[45,57–61]. The increase in T-cell specific cytokines, alongside an increase in CXCL2, a potent granulocyte chemokine, typically secreted by activated macrophages, are indicative of bacterial infection and are likely to recruit a variety of leukocytes into the tumor microenvironment beyond those assayed in this study. This indicates that the bacteria are likely to induce the production of these cytokines at the site of injection but are ultimately sequestered locally to initiate a broader systemic immune response directed at the foreign bacteria, and indirectly against the tumor. Taken together, this data suggests that injections of MSR-1 bacteria can be used as a potent $T_h$ 2/17 immunomodulator in the context of improving cancer therapy.

Nanoparticles are well established carriers for drugs that are insoluble or unstable in the circulation, enabling their use to potentially improve the efficacy of immunotherapeutic bacteria. Indeed, studies have shown that nanoparticle-based drug delivery systems, including nanoliposomes, can be combined with bacteria to yield better cancer treatments in mice, specifically where the bacteria can improve the transport of conjugated nanoparticles into tumors *via* their flagella[14]. This hitchhiking strategy can facilitate the delivery of therapeutic cargo to hard-to-access tumor regions, as observed with the accumulation of the MLC in the core of YUMM 1.7 spheroids, which is likely driven by the presence of an oxygen gradient, as hypoxic and necrotic regions typically occur towards the core of a spheroid as the cells multiply[62]. Since MSR-1 bacteria are known microaerophiles, they prefer regions of low oxygen tension, however, other reasons for their targeting to the core regions of spheroids may include the bacteria avoiding $CO_2$ rich media, as well as the possible presence of a chemotactic gradient, such as a more acidic pH towards the core. It is important to note that the presence of conjugated nanoparticles onto the bacterial surface did not prevent the bacterial opsonization when incubated in human plasma (data not shown). Since CuET blocks the p97-NPL4 complex, misfolded proteins accumulate in the ER of the cell causing proteotoxic stress and translational arrest thereby initiating the unfolded protein response[40]. This effect could be extrapolated in vivo, as cells of the MPS system are responsible for clearing opsonized bacteria *via* phagocytosis, mainly in the liver and lymphoid tissues. Therefore, an induction of temporary ER stress from their uptake of CuET from bacterial-conjugated nanoparticles, could result in a temporary decrease in phagocytosis and might allow longer circulation time for bacteria resulting in higher bacterial counts and penetration inside tumors. The nanoshielding effect would be interesting to study in a broader context of nanoparticle-based drug delivery, whereby instead of depleting scavenger cells, their phagocytic ability could be temporarily disabled to allow other therapeutic micro/nanoparticles to accumulate into the tumors. Other studies assessing a wide variety of drug-loaded nanoparticles would be welcomed to confirm the nanoshielding hypothesis. It remains to be seen to what extent the magnitude of this effect can be attributed to the induction of ER stress, but other compounds known to induce ER stress, e.g., bortezomib, might help address the mechanism of action.

Overall, the data suggests that a larger number of nanoparticles are delivered into tumors when MSR-1 bacteria are present, and equivalently, there are more live bacteria present in tumors in the presence of LP-CuET, likely due to a complementary effect. The MPS system may be challenged in its ability recognize and engulf the nanoplexed bacteria, thus allowing for a distinct biodistribution profile when the bacteria are combined with nanoparticles as a drug delivery strategy. In addition, recent studies have shown that nanoparticles tend to be sequestered by the MPS to a larger extent at doses < $10^{12}$ nanoparticles due to the ability of nanoparticles to saturate scavenger cells at higher doses[29]. A similar effect is likely taking place in this case, where phagocytic and scavenger cells are being saturated when bacteria are being delivered alongside the nanoshields, and vice versa. Notably, there was no difference in the bacterial colonization or treatment efficacy when MSR-1 bacteria were delivered with empty liposomes compared to MSR-1 alone (data not shown), indicating that LP-CuET plays a role in improving the bacterial efficacy and biodistribution in lung metastases when injected IV, with the potential to modulate the immune response by altering the cytokine profile in mouse plasma (Supplementary Fig. 22), which warrants further exploration.

Using *M. gryphiswaldense* as a potent anti-cancer agent and immunomodulator, we showed that the bacteria can also be used as drug-delivery vectors using surface-bound nanoparticles. The cell hitchhiking strategy can also reduce the premature clearance of bacteria from the bloodstream, leading to improved tumor targeting and enhanced treatment efficacy in murine models of melanoma. While this study employed liposomes loaded with a single drug, the combination of various types of nanoparticles loaded with different therapeutic agents alongside engineered bacteria, or other immunomodulatory microorganisms, could open the door to a myriad of therapeutic possibilities in oncology. By employing bacterial hitchhiking of nanoparticles, we can envision delivering a multitude of micro- and nanoscale structures more efficiently to their intended targets and ultimately improving cancer treatments.

## Methods

### Materials

B16F10 (RRID:CVCL_0159) and YUMM 1.7 (RRID:CVCL_JK16) cell lines were obtained from Dr. Ian Watson. THP-1 (RRID:CVCL_0006) cells (TIB-202), Vitamin (MD-VS™) and Trace Mineral (MD-TMS™) supplements were purchased from the American Type Culture Collection (Manassas, VA). *E. coli* strain DH5α cells, CD3 (17A2), F4/80 (BM8), and CD45r (RA3-6B2), cell culture flasks (T75) and dishes, glass coverslips, 6- and 96-well plates, hematoxylin, eosin, mounting solution, formaldehyde solution, penicillin–streptomycin, trypsin, Dulbecco's Modified Eagle Medium (DMEM), Roswell Park Memorial Institute (RPMI) 1640, non-essential amino acids (NEAA), fetal bovine serum (FBS), NucBlue™ Live ReadyProbes reagent (Hoechst 33342), Texas Red™ 1,2-dihexadecanoyl-sn-glycero-3-phosphoethanolamine (DHPE), and human ELISA kits were obtained from Thermo Fisher Scientific (Waltham, MA, USA). 96-well glass bottom plates were purchased from Cellvis (Mountain View, CA). Scale-view-S4, an optical clearing reagent, was obtained from FUJIFILM Wako Pure Chemical Corporation (Richmond, VA). *M. gryphiswaldense* strain MSR-1 cells were obtained from the Japanese Collection of Microorganisms, Riken BRC (Japan). Copper (II) diethyldithiocarbamate was purchased from Tokyo Chemical Industry (Japan). 1,2-distearoyl-sn-glycero-3-phosphocholine (DSPC), 1,2-distearoyl-sn-glycero-3-phosphoethanolamine-N-[carboxy(polyethylene glycol)-2000] (DSPE-$PEG_{2000}$-COOH) and 1,2-distearoyl-sn-glycero-3-phosphoethanolamine-N-[methoxy(polyethylene glycol)-2000] (DSPE-$PEG_{2000}$-OMe) were purchased from Avanti Polar Lipids (Alabaster, AL, USA). Anhydrous ethanol was purchased from Commercial Alcohols (Boucherville, QC, Canada). HRP goat-anti rat IgG detection kit, endogenous blocking solution, and DAB substrate were purchased from Vector Laboratories (Newark, CA). Silicon dioxide QSensors (QSX 303) were purchased from NanoScience Instruments (Phoenix, AZ). 8-week-old C57BL/6 mice of both sexes were purchased from Charles River Laboratories (Wilmington, MA). αPD1 (RMP1-14), αCTLA4 (9D9), and isotype IgG2a (2A3) and IgG2b (MPC-11) control antibodies, and 6.5 pH dilution buffer (IP0065) were purchased from Bio X Cell (Lebanon, NH). All other materials and chemicals, including the high-sensitivity T cell Milliplex® kit (MHSTCMAG-70K), were purchased from Millipore Sigma (Burlington, MA).

### Bacterial cell culture

*M. gryphiswaldense* strain MSR-1 bacteria were cultured at 30 °C in a slightly modified *Magnetospirillum* growth medium (mMSGM, Supplementary Table 1) under microaerophilic conditions (1% $O_2$) in sealed serum flasks, and on 1% mMSGM agar plates for at least 48 h. *E. coli* DH5α cells from a single colony were grown overnight in Lennox lysogeny broth (LB) media under shaking conditions, and on 1.5% LB agar plates at 37 °C.

### Mammalian cell culture

B16F10 and YUMM 1.7 cells were cultured in T75 flasks containing DMEM, and THP-1 cells were cultured in non-adherent T75 flasks

containing RPMI-1640. Cells were maintained at 37 °C in an incubator with a humidified atmosphere containing 5% $CO_2$. Both DMEM and RPMI-1640 were supplemented with 10% (v/v) fetal bovine serum (FBS), 1% (v/v) of non-essential amino acids (NEAA) and 1% (v/v) penicillin/streptomycin. Antibiotic-free media was used when bacteria were co-cultured with mammalian cells. For spheroid formation, YUMM 1.7 cells were added to a low adhesion 96-well U-bottom microplate at a density of $10^4$ cells per well, and cells were allowed to aggregate to form spheroids for 24 h. The spheroids were then detached from the bottom of each well by pipetting fresh media multiple times. The spheroids were then transferred to a low adhesion 6-well plate that was placed in the incubator on a revolving shaker (100 RPM) for 48 h. Cytotoxicity was evaluated by seeding cancer cells in 96-well plates at a density of 10,000 cells per well and incubated overnight. The cells were then treated at various concentrations with MSR-1 or MLC. Cells were fixed with 50% trichloroacetic acid, stained with 0.4% suflorhodamine B, and resuspended in TRIS buffer (10 mM) at a final volume of 200 µL per well, and the optical density was measured at 492 nm.

### Mouse experiments

C57BL/6 male and female mice (25–30 g, 12 weeks old) were acclimated to their environment and maintained under specific pathogen-free conditions. Mice were injected subcutaneously (dorsally) or intravenously (tail vein) with $5 \times 10^5$ or $3 \times 10^5$ B16F10 cells in 100 µL PBS to establish the ectopic or metastatic mouse models, respectively. Mice that did not establish subcutaneous tumors by the treatment date were excluded from the experiment. For ectopic models, tumors became visible 7 days following implantation; mice were randomized by weight into the following groups: vehicle (PBS), MSR-1 ($10^8$ CFU), DH5α ($10^8$ CFU), isotype (100 µg IgG controls for each antibody), and αPD1 + αCTLA4 (100 µg for each antibody). Treatments were administered in a non-blinded setting in 100 µL peritumorally (PT) except for the antibodies, which were administered *via* intraperitoneal (IP) injections according to the treatment schedule illustrated in Fig. 2A. Tumor growth was monitored every second day through width (W) and length (L) measurements using a standard electronic caliper. Tumor volume (V) was calculated using the following formula: $V = W^2 \times L$. Body weights were monitored every second day. Endpoint tumor volume was defined as 2 $cm^3$ according to the Facility Animal Care Committee (FACC) guidelines. Survival of the tumor-bearing mice was evaluated using Kaplan-Meier analysis. For the metastatic model, mice were randomized by weight into the following groups: vehicle (empty LP), liposomal CuET (LP-CuET, 1 mg/kg), MSR-1 ($10^9$ CFU), MLC ($10^9$ CFU + LP CuET). Treatments were administered in 100 µL intravenously (IV) according to the treatment schedule in Fig. 6A. At endpoint, the mice were sacrificed, and their lungs were isolated and perfused *via* the trachea with Fekete's solution containing 1% formalin, 70% ethanol and 4% acetic acid. The lungs were then immersed in Fekete's solution and fixed for at least 48 h to visualize and count the pigmented metastatic lesions. All experimental procedures were performed in accordance with the FACC of the McGill University Health Center, Montreal, QC, Canada (AUP 7946). Since primary melanomas are normally cutaneous lesions, we refer to our subcutaneous model as ectopic.

### Histology and immunohistochemistry

Organs and tumors from treated mice were removed at endpoint, fixed in 10% buffered formalin for at least 48 h, embedded in paraffin, and sectioned at a thickness of 5 µm. Hematoxylin and eosin (H&E) staining was performed manually using a standard protocol, and immunostaining was performed according to manufacturer guidelines using the goat-anti rat ImmPRESS® HRP polymer detection kit (VECTMP744415). Tumor tissue sections were stained with primary monoclonal antibodies against CD45R, CD3, and F4/80 staining for B cells, T cells, and macrophages, respectively. Pictures were obtained using a Zeiss Axioskop 2 digital pathology microscope (Oberkochen, Germany) at 20x magnification.

### Cytokine Expression Assays

THP-1 cells were seeded in 6-well plates at a density of $1 \times 10^6$ cells per well and differentiated into M0 macrophages with 10 ng/mL of phorbol 12-myristate 13-acetate (PMA) for 48 h. Attached cells were then rested in PMA-free media for 24 h. Rested cells were washed thrice with PBS and $1 \times 10^7$ CFU of MSR-1 bacteria were added in antibiotic-free media and incubated for 3, 6, 12 and 24 h. Standard ELISAs against human TNFα (88-7346-22) and IL-6 (88-7066-22) were performed using filtered (0.45 µm) media supernatants according to manufacturer instructions. To evaluate cytokine production in mice after treatment, mouse plasma was isolated 24 h after treatment, or at experimental endpoint, and was used to perform a multiplexed ELISA on a variety of relevant cytokines using a high-sensitivity T cell Milliplex® kit (MHSTCMAG-70K) on the Luminex MAGPIX® system according to manufacturer instructions.

### Liposome fabrication and bacterial coupling

Liposomal copper diethyldithiocarbamate (LP-CuET) was synthesized as previously described[63]. Briefly, a lipid mixture containing DSPC/DSPE-$PEG_{2000}$-COOH/DSPE-$PEG_{2000}$-OMe/Cholesterol/CuET (molar ratio of 4/0.1/0.1/2.5/1) was added to 5 mL of pure ethanol in a closed container and was heated to 50 °C until complete CuET dissolution. The hot ethanol mixture was then injected into 45 mL of rapidly stirred ultrapure water at a constant rate. The resulting solution was transferred to a rotary evaporator to remove the ethanol and concentrate the nanoparticles. The solution was suspended in PBS, filter sterilized (0.22 µm), and stored at 4 °C for up to three months. Fluorescent liposomes were synthesized in the same manner with the addition of 1% (mol/mol) Texas Red™ DHPE. Empty liposomes (no CuET) were used as vehicle controls. For liposomal coupling to bacteria, 4-(4,6-Dimethoxy-1,3,5-triazin-2-yl)-4-methylmorpholinium chloride (DMTMM) was added to the nanoparticle solution at a DMTMM to DSPE-$PEG_{2000}$-COOH ratio of 2:1 to activate the carboxylic acids. The nanoparticle solution was then added to the bacteria in excess in PBS and incubated for 30 min.

### Bacterial phagocytosis assay

THP-1 monocytes were seeded in 6-well plates at a density of $1 \times 10^6$ cells per well and differentiated into M0 macrophages with 10 ng/mL of PMA for 48 h; attached cells were then rested in PMA-free media for 24 h. Rested cells were washed thrice with PBS and incubated with $10^6$ CFU of MSR-1, empty liposomes + $1 \times 10^6$ CFU of MSR-1, or LP-CuET + $1 \times 10^6$ CFU of MSR-1 for 3 h in antibiotic-free media. Viable THP-1 cells were then washed thrice with PBS, resuspended using trypsin, and washed again thrice with PBS at 200 RCF for 5 min. The THP-1 cells were then lysed and plated on 1% mMSGM agar plates for colony counting.

### Fluorescence and confocal microscopy

Fluorescence microscopy images of MSR-1 bacteria with or without captured LP-CuET nanoparticles labeled with Texas Red™ were obtained using the Nikon Eclipse TE2000U epifluorescence microscope (Tokyo, Japan) at a 40x magnification after the bacteria have been washed thrice with PBS and captured onto a poly-L-lysine coated glass slide. Confocal images of isolated tumor tissue from mice injected peritumorally with 1 mg/kg fluorescent LP-CuET or 1 mg/kg fluorescent LP-CuET + $10^8$ CFU of MSR-1 bacteria were captured at a 40x magnification using the Carl Zeiss LSM 800 laser scanning microscope.

Spheroid confocal imaging was performed according to a previously established protocol[64]. YUMM 1.7 spheroids were treated with 1 µM fluorescent LP-CuET, $10^7$ CFU of rhodamine B isothiocyanate (RBITC)-labeled MSR-1 bacteria, or the complex of fluorescent LP-CuET attached to $10^7$ CFU of MSR-1 bacteria. Bacteria were labeled with RBITC by incubation in 0.1 M bicarbonate solution (pH 9.0) for 30 min. After the treatments, spheroids were collected and fixed with 4% (v/v) paraformaldehyde for 30 min and nuclei were stained with Hoechst 33342 (1:1000) for 15 min. Scaleview-S4 clearing solution was added to the spheroids prior to the imaging. Pictures were acquired using Opera Phenix™ high-content

screening system (Perkin Elmer) equipped with microlens-enhanced spinning disk using water immersion objectives. For zone analysis of the spheroids, the "Find region" and resized region modules of the software were used. The physical characteristics of the spheroids were measured using Harmony® 4.9 imaging and analysis software. The "Find region" module was used to detect the boundaries of the spheroids for the nanoparticle penetration analysis into the core of the spheroids defined at a boundary zone of 30 μm from the surface.

### Bacterial biodistribution

Mice bearing subcutaneous B16F10 tumors were injected IV with $10^9$ CFUs of MSR-1 bacteria with and without 1 mg/kg LP-CuET. After 24 h, the mice were sacrificed and their organs and tumors were collected into sterile tubes, weighed, homogenized, and plated on parafilm-sealed 1% mMSGM agar plates at 30 °C for 10 days for colony counting.

### Ex vivo fluorescence imaging

Mice were injected dorsally with $5 \times 10^5$ YUMM 1.7 cells to establish subcutaneous tumors or intravenously with $3 \times 10^5$ B16F10 cells to establish lung lesions. When the subcutaneous tumors reached a volume of 500 $mm^3$, or on day 15 post tumor cell injection for the metastatic model, mice were intravenously treated with 1 mg/kg fluorescent (Texas Red™) LP-CuET nanoparticles or $10^9$ CFU of bacteria with 1 mg/kg fluorescent LP-CuET nanoparticles in 100 μL. Imaging was performed on ex vivo mouse organs 3 h post-IV injection using the Bruker In-Vivo Xtreme (Billerica, MA). YUMM 1.7 tumors were used for biodistribution studies to allow for better visualization and quantification of fluorescence images since B16F10 cells produce a significant amount of melanin, which may interfere with the imaging process.

### Electron microscopy

MSR-1 bacteria with and without captured liposomes on the surface were fixed with 3% glutaraldehyde in PBS and deposited onto a round poly-L-lysine coated glass slide for 30 min. The slide was rinsed in ultrapure water and dehydrated in a series of ethanol solutions (30–100% v/v). The slides were then placed in a metal sample holder for critical point drying using the Leica Microsystems EM CPD300 (Wetzlar, Germany). Afterwards, the slides were mounted on metal stubs and sputter coated with platinum (5 nm thickness using the Leica Microsystems EM ACE600) before performing scanning electron microscopy (SEM) imaging at an accelerating voltage of 10 kV using the FEI Quanta 450 FE-SEM (Hillsboro, OR). For transmission electron microscopy (TEM), liposomes or bacteria were drop cast on a carbon-copper grid and stained with uranyl acetate for 30 s for contrast. The imaging was performed using the Thermo Scientific Talos F200X G2 (S) at a voltage of 200 kV.

### Nanoparticle capture analysis

To quantify the capture of nanoparticles onto the surface of bacteria, approximately $10^{12}$ LP-CuET (DMTMM-activated) nanoparticles were incubated with $10^9$ CFU of MSR-1 bacteria for 1 h. The bacteria were pelleted at 5000 RCF for 20 min, and the number of leftover nanoparticles was determined in the supernatant *via* Nanoparticle Tracking Analysis (NTA) using the Malvern Nanosight NS300 (Malvern, UK). The difference yields the number of nanoparticles captured by the bacteria. To quantify the stability of captured surface nanoparticles, MSR-1 were washed twice with PBS after nanoparticle capture, and the release of nanoparticles into the supernatant was quantified by NTA minus the release of outer membrane vesicles from the control bacteria without attached nanoparticles.

### Quartz crystal microbalance with dissipation measurements

$SiO_2$ sensors were cleaned according to manufacturer instructions, treated with UV/ozone for 10 min using the Plasma Etch (Carson City, NV) and coated with poly-L-lysine (0.05%) for 30 min before use. The sensors were then mounted in flow chambers using the Q-Sense E4, Biolin Scientific (Gothenburg, Sweden), and MSR-1 bacteria were captured on the sensor overnight to ensure they form a stable monolayer before DMTMM-activated or non-activated LP-CuET liposomes were flown to assess liposome capture kinetics. In a reverse experiment, DMTMM-activated and non-activated LP-CuET liposomes were captured on the surface first before bacteria were flown to assess the adhesion of bacteria onto a liposomal monolayer. All experiments were performed at room temperature with a constant flow rate of 10 μL/min.

### Atomic force microscopy

DMTMM-activated LP-CuET nanoparticles were deposited onto a poly-L-lysine coated glass slide for 10 min. The glass slide was rinsed with PBS and immediately after, $10^7$ CFU of MSR-1 bacteria in PBS were incubated on the slide for 30 min. The surface was then fixed with 4% paraformaldehyde for 30 min, washed with ultrapure water and dried under nitrogen gas. The imaging was carried out using the Multi Mode™ AFM (Bruker) in the Quantitative Nanomechanical mode (in air) using a sharp silicon nitride lever (SNL-10, Bruker) with a spring constant of 0.12 N/m.

### Statistical analysis

Experiments were carried out independently in at least technical and biological triplicates ($n \geq 3$). Student's t-test with Welch's correction, and Brown–Forsythe and Welch's one-way ANOVA with Dunnett's 3 T correction with multiple comparisons were used to assess the statistical significance between groups at 95% confidence (two-sided). The data were considered significant when $p < 0.05$ (* < 0.05, ** < 0.01, *** < 0.005, **** < 0.0001). Sample size was determined based on power calculations performed to account for the normal variance in the tumor models. All statistics were performed using the Prism GraphPad 10 software.

## Data availability

Additional data used and/or analyzed during the current study are available from the corresponding author upon reasonable request.

Received: 25 July 2024; Accepted: 29 December 2024;
Published online: 24 January 2025

## References

1. Hou, J. Z. et al. Novel agents and regimens for hematological malignancies: recent updates from 2020 ASH annual meeting. *J Hematol Oncol* **14**, 66 (2021).
2. McKeown, S. R. Defining normoxia, physoxia and hypoxia in tumours-implications for treatment response. *Br J Radiol* **87**, 20130676 (2014).
3. Duong, M. T., Qin, Y., You, S. H. & Min, J. J. Bacteria-cancer interactions: bacteria-based cancer therapy. *Exp Mol Med* **51**, 1–15 (2019).
4. Ganai, S., Arenas, R. B., Sauer, J. P., Bentley, B. & Forbes, N. S. Attenuated salmonella typhimurium effectively targets breast cancer metastases. *Ann Surg Oncol* **16**, 18–19 (2009).
5. Dhital, S., Deo, P., Stuart, I. & Naderer, T. Bacterial outer membrane vesicles and host cell death signaling. *Trends Microbiol* **29**, 1106–1116 (2021).
6. Kim, O. Y. et al. Bacterial outer membrane vesicles suppress tumor by interferon-gamma-mediated antitumor response. *Nat Commun* **8**, 626 (2017).
7. Li, Y. et al. Bacterial outer membrane vesicles presenting programmed death 1 for improved cancer immunotherapy via immune activation and checkpoint inhibition. *ACS Nano* **14**, 16698–16711 (2020).
8. Huang, X. et al. Bacteria-based cancer immunotherapy. *Adv Sci (Weinh)* **8**, 2003572 (2021).
9. Forbes, N. S. et al. White paper on microbial anti-cancer therapy and prevention. *J Immunother Cancer* **6**, 78 (2018).
10. Rismani Yazi, S., Nosrati, R., Stevens, C. A., Vogel, D. & Escobedo, C. Migration of magnetotactic bacteria in porous media. *Biomicrofluidics* **12**, 011101 (2018).
11. Gurbatri, C. R. et al. Engineered probiotics for local tumor delivery of checkpoint blockade nanobodies. *Sci Transl Med* **12** (2020).

12. Chowdhury, S. et al. Programmable bacteria induce durable tumor regression and systemic antitumor immunity. *Nat Med* **25**, 1057–1063 (2019).
13. Taherkhani, S., Mohammadi, M., Daoud, J., Martel, S. & Tabrizian, M. Covalent binding of nanoliposomes to the surface of magnetotactic bacteria for the synthesis of self-propelled therapeutic agents. *ACS Nano* **8**, 5049–5060 (2014).
14. Felfoul, O. et al. Magneto-aerotactic bacteria deliver drug-containing nanoliposomes to tumour hypoxic regions. *Nat Nanotechnol* **11**, 941–947 (2016).
15. Suh, S. et al. Nanoscale bacteria-enabled autonomous drug delivery system (NanoBEADS) enhances intratumoral transport of nanomedicine. *Adv Sci (Weinh)* **6**, 1801309 (2019).
16. Wang, B. et al. Magnetotactic bacteria-based drug-loaded micromotors for highly efficient magnetic and biological double-targeted tumor therapy. *ACS Appl Mater Interfaces* **15**, 2747–2759 (2023).
17. Mirkhani, N., Christiansen, M. G., Gwisai, T., Menghini, S. & Schuerle, S. Spatially selective delivery of living magnetic microrobots through torque-focusing. *Nature Communications* **15**. https://doi.org/10.1038/s41467-024-46407-4 (2024).
18. Gwisai, T. et al. Magnetic torque-driven living microrobots for increased tumor infiltration. *Sci Robot* **7**, eabo0665 (2022).
19. Xiang, Z. et al. Drug-internalized bacterial swimmers for magnetically manipulable tumor-targeted drug delivery. *Nanoscale* **12**, 13513–13522 (2020).
20. Gwisai, T. et al. Engineering Living Immunotherapeutic Agents for Improved Cancer Treatment. *Adv Ther-Germany* **7** (2024).
21. Toso, J. F. et al. Phase I study of the intravenous administration of attenuated Salmonella typhimurium to patients with metastatic melanoma. *J Clin Oncol* **20**, 142–152 (2002).
22. Thornlow, D. N., Brackett, E. L., Gigas, J. M., Van Dessel, N. & Forbes, N. S. Persistent enhancement of bacterial motility increases tumor penetration. *Biotechnol Bioeng* **112**, 2397–2405 (2015).
23. Toley, B. J. & Forbes, N. S. Motility is critical for effective distribution and accumulation of bacteria in tumor tissue. *Integr Biol-Uk* **4**, 165–176 (2012).
24. Broadley, S. P. et al. Dual-track clearance of circulating bacteria balances rapid restoration of blood sterility with induction of adaptive immunity. *Cell Host Microbe* **20**, 36–48 (2016).
25. Kraft, B. D. et al. Development of a novel preclinical model of pneumococcal pneumonia in nonhuman primates. *Am J Respir Cell Mol Biol* **50**, 995–1004 (2014).
26. Thamm, D. H. et al. Systemic administration of an attenuated, tumor-targeting Salmonella typhimurium to dogs with spontaneous neoplasia: phase I evaluation. *Clin Cancer Res* **11**, 4827–4834 (2005).
27. McBride, M. A. et al. Immune checkpoints: novel therapeutic targets to attenuate sepsis-induced immunosuppression. *Front Immunol* **11**, 624272 (2020).
28. Patil, N. K., Guo, Y., Luan, L. & Sherwood, E. R. Targeting Immune Cell Checkpoints during Sepsis. *Int J Mol Sci* **18**. https://doi.org/10.3390/ijms18112413 (2017).
29. Ouyang, B. et al. The dose threshold for nanoparticle tumour delivery. *Nat Mater* **19**, 1362–1371 (2020).
30. Benoit, M. R. et al. Visualizing implanted tumors in mice with magnetic resonance imaging using magnetotactic bacteria. *Clin Cancer Res* **15**, 5170–5177 (2009).
31. Amor, M. et al. Magnetotactic Bacteria Accumulate a Large Pool of Iron Distinct from Their Magnetite Crystals. *Appl Environ Microb* **86**. https://doi.org/10.1128/AEM.01278-20 (2020).
32. Schuler, D. & Baeuerlein, E. Iron-limited growth and kinetics of iron uptake in Magnetospirillum gryphiswaldense. *Arch Microbiol* **166**, 301–307 (1996).
33. Wang, Q. et al. Physiological characteristics of Magnetospirillum gryphiswaldense MSR-1 that control cell growth under high-iron and low-oxygen conditions. *Sci Rep* **7**, 2800 (2017).
34. Menghini, S., Ho, P. S., Gwisai, T. & Schuerle, S. Magnetospirillum magneticum as a Living Iron Chelator Induces TfR1 Upregulation and Decreases Cell Viability in Cancer Cells. *International Journal of Molecular Sciences* **22**. https://doi.org/10.3390/ijms22020498 (2021).
35. Menghini, S., Vizovisek, M., Enders, J. & Schuerle, S. Magnetospirillum magneticum triggers apoptotic pathways in human breast cancer cells. *Cancer Metab* **11**. https://doi.org/10.1186/s40170-023-00313-3 (2023).
36. Jiang, X. P. & Elliott, R. L. Decreased iron in cancer cells and their microenvironment improves cytolysis of breast cancer cells by natural killer cells. *Anticancer Res* **37**, 2297–2305 (2017).
37. Sottile, R. et al. Iron and ferritin modulate MHC class I expression and NK cell recognition. *Front Immunol* **10**, 224 (2019).
38. Caron, G. et al. Direct stimulation of human T cells via TLR5 and TLR7/8: flagellin and R-848 up-regulate proliferation and IFN-gamma production by memory CD4+ T cells. *J Immunol* **175**, 1551–1557 (2005).
39. Trinchieri, G. & Sher, A. Cooperation of Toll-like receptor signals in innate immune defence. *Nat Rev Immunol* **7**, 179–190 (2007).
40. Skrott, Z. et al. Alcohol-abuse drug disulfiram targets cancer via p97 segregase adaptor NPL4. *Nature* **552**, 194–199 (2017).
41. Pan, M. et al. Seesaw conformations of Npl4 in the human p97 complex and the inhibitory mechanism of a disulfiram derivative. *Nat Commun* **12**, 121 (2021).
42. Hao, Q. et al. A non-canonical role of the p97 complex in RIG-I antiviral signaling. *EMBO J* **34**, 2903–2920 (2015).
43. Cao, K., Nakajima, R., Meyer, H. H. & Zheng, Y. X. The AAA-ATPase Cdc48/p97 regulates spindle disassembly at the end of mitosis. *Cell* **115**, 355–367 (2003).
44. Vaz, B., Halder, S. & Ramadan, K. Role of p97/VCP (Cdc48) in genome stability. *Front Genet* **4**, 60 (2013).
45. Majera, D. et al. Targeting the NPL4 Adaptor of p97/VCP Segregase by Disulfiram as an Emerging Cancer Vulnerability Evokes Replication Stress and DNA Damage while Silencing the ATR Pathway. *Cells-Basel* **9**. https://doi.org/10.3390/cells9020469 (2020).
46. Lam, M., Marsters, S. A., Ashkenazi, A. & Walter, P. Misfolded proteins bind and activate death receptor 5 to trigger apoptosis during unresolved endoplasmic reticulum stress. *Elife* **9**. https://doi.org/10.7554/eLife.52291 (2020)
47. Liu, D., Jenkins, R. W. & Sullivan, R. J. Mechanisms of resistance to immune checkpoint blockade. *Am J Clin Dermatol* **20**, 41–54 (2019).
48. Harrington, K. J. et al. Clinical development of talimogene laherparepvec (T-VEC): a modified herpes simplex virus type-1-derived oncolytic immunotherapy. *Expert Rev Anticancer Ther* **15**, 1389–1403 (2015).
49. Tawbi, H. A. et al. Relatlimab and Nivolumab versus Nivolumab in Untreated Advanced Melanoma. *N Engl J Med* **386**, 24–34 (2022).
50. Shen, J. et al. Inflamed immune phenotype predicts favorable clinical outcomes of immune checkpoint inhibitor therapy across multiple cancer types. *J Immunother Cancer* **12**. https://doi.org/10.1136/jitc-2023-008339 (2024).
51. Wehbe, M. et al. Nanoscale reaction vessels designed for synthesis of copper-drug complexes suitable for preclinical development. *PLoS One* **11**, e0153416 (2016).
52. Wehbe, M. et al. Development and optimization of an injectable formulation of copper diethyldithiocarbamate, an active anticancer agent. *Int J Nanomedicine* **12**, 4129–4146 (2017).
53. Jiang, G., Xiang, Z. & Fang, Q. Engineering magnetotactic bacteria MVs to synergize chemotherapy, ferroptosis and immunotherapy for augmented antitumor therapy. *Nanoscale Horiz* **8**, 1062–1072 (2023).
54. Ross, S. H. & Cantrell, D. A. Signaling and Function of Interleukin-2 in T Lymphocytes. *Annu Rev Immunol* **36**, 411–433 (2018).
55. Mills, K. H. G. IL-17 and IL-17-producing cells in protection versus pathology. *Nat Rev Immunol* **23**, 38–54 (2023).
56. Walker, J. A. & McKenzie, A. N. J. T(H)2 cell development and function. *Nat Rev Immunol* **18**, 121–133 (2018).

57. Mattes, J. et al. Immunotherapy of cytotoxic T cell-resistant tumors by T helper 2 cells: an eotaxin and STAT6-dependent process. *J Exp Med* **197**, 387–393 (2003).
58. Eftimie, R., Bramson, J. L. & Earn, D. J. Modeling anti-tumor Th1 and Th2 immunity in the rejection of melanoma. *J Theor Biol* **265**, 467–480 (2010).
59. Lorvik, K. B. et al. Adoptive transfer of tumor-specific Th2 cells eradicates tumors by triggering an in situ inflammatory immune response. *Cancer Res* **76**, 6864–6876 (2016).
60. Zhang, S. et al. CD4 T-cell-mediated anti-tumor immunity can be uncoupled from autoimmunity the STAT4/STAT6 signaling axis. *Eur J Immunol* **39**, 1252–1259 (2009).
61. Jacenik, D., Karagiannidis, I. & Beswick, E. J. Th2 cells inhibit growth of colon and pancreas cancers by promoting anti-tumorigenic responses from macrophages and eosinophils. *Br J Cancer* **128**, 387–397 (2023).
62. Kirsh, S. M., Pascetta, S. A. & Uniacke, J. Spheroids as a 3D Model of the Hypoxic Tumor Microenvironment. *Methods Mol Biol* **2614**, 273–285 (2023).
63. Paun, R. A. et al. One-Step Synthesis of Nanoliposomal Copper Diethyldithiocarbamate and Its Assessment for Cancer Therapy. *Pharmaceutics* **14**. https://doi.org/10.3390/pharmaceutics14030640 (2022).
64. Rasouli, R., Paun, R. A. & Tabrizian, M. Sonoprinting nanoparticles on cellular spheroids via surface acoustic waves for enhanced nanotherapeutics delivery. *Lab Chip* **23**, 2091–2105 (2023).


## Acknowledgements

The authors acknowledge the financial support of the Canadian Institute of Health Research (CIHR) and the Natural Sciences and Engineering Research Council (NSERC) via the Project and Discovery Grant Programs, the Canada Research Chair – Tier 1 in Regenerative Medicine and Nanomedicine to MT, as well as Fonds de Recherche du Quebec – Santé (FRQS) scholarships to RAP and DCD. The authors would like to acknowledge Dr. Ian Watson and Dr. Marcus Bosenberg for providing our laboratory with the melanoma cell lines. The authors thank Dr. Reza Rasouli, Nicholas van der Sanden, as well as the Facility for Electron Microscopy Research (FEMR) and the Animal Resource Division (ARD) of the Research Institute of the McGill University Hospital Center (RI-MUHC) staff for their input and help with experiments.

## Author contributions

R.A.P. – conceptualization, methodology, formal analysis and experimentation, data curation, methodology and manuscript writing. D.C.D. – experimentation, methodology, review and editing of the manuscript. L.L. – experimentation, methodology, review and editing of the manuscript. D.R. – conceptualization, investigation, supervision, review and editing of the manuscript. M.T. – conceptualization, investigation, supervision, project administration, review and editing of the manuscript. All authors have given approval to the final version of the manuscript.

## Competing interests

R.A.P., D.R., and M.T. are named inventors on a pending patent application.

## Additional information

**Supplementary information** The online version contains supplementary material available at https://doi.org/10.1038/s44385-024-00006-6.

**Correspondence** and requests for materials should be addressed to Maryam Tabrizian.